Journal of Neuroscience Methods 411 (2024) 110273

Contents lists available at ScienceDirect

Journal of Neuroscience Methods

journal homepage: www.elsevier.com/locate/jneumeth

NeuroQuantify – An image analysis software for detection and quantification of neuron cells and neurite lengths using deep learning

Ka My Dang [a,b,*], Yi Jia Zhang [c], Tianchen Zhang [c], Chao Wang [c], Anton Sinner [a], Piero Coronica [d], Joyce K.S. Poon [a,b,c,*]

[a] Max Planck Institute of Microstructure Physics, Weinberg 2, Halle D-06120, Germany
[b] Max Planck-University of Toronto Centre for Neural Science and Technology, Canada
[c] Department of Electrical and Computer Engineering, University of Toronto, 10 King's College Rd., Toronto, Ontario M5S 3G4, Canada
[d] Max Planck Computing and Data Facility, Gießenbachstraße 2, Garching 85748, Germany

ARTICLE INFO

Keywords:
Deep learning
Microscopy images
Neuronal imaging
Neuron segmentation
Neuron quantification

ABSTRACT

Background: The segmentation of cells and neurites in microscopy images of neuronal networks provides valuable quantitative information about neuron growth and neuronal differentiation, including the number of cells, neurites, neurite length and neurite orientation. This information is essential for assessing the development of neuronal networks in response to extracellular stimuli, which is useful for studying neuronal structures, for example, the study of neurodegenerative diseases and pharmaceuticals.
New method: We have developed NeuroQuantify, an open-source software that uses deep learning to efficiently and quickly segment cells and neurites in phase contrast microscopy images.
Results: NeuroQuantify offers several key features: (i) automatic detection of cells and neurites; (ii) post-processing of the images for the quantitative neurite length measurement based on segmentation of phase contrast microscopy images, and (iii) identification of neurite orientations.
Comparison with existing methods: NeuroQuantify overcomes some of the limitations of existing methods in the automatic and accurate analysis of neuronal structures. It has been developed for phase contrast images rather than fluorescence images. In addition to typical functionality of cell counting, NeuroQuantify also detects and counts neurites, measures the neurite lengths, and produces the neurite orientation distribution.
Conclusions: We offer a valuable tool to assess network development rapidly and effectively. The user-friendly NeuroQuantify software can be installed and freely downloaded from GitHub at https://github.com/StanleyZ0528/neural-image-segmentation.

1. Introduction

Quantitative analysis of neuronal cell structures is important for biomedical and pharmaceutical research, such as the determination of drug uptake and toxicity (Lilienberg et al., 2021; Pai et al., 2022). Typical analysis involves monitoring changes in the culture properties, such as the neuron numbers, neurite outgrowth directions, and neurite differentiation, to assess the physiological state of the neuronal culture (Dravid et al., 2021). Changes in the neuronal networks are indicative of neuronal development in response to extracellular stimuli (e.g., biochemical, electrical, optical, mechanical, and topographical) (Graves et al., 2009; Sacher et al., 2022; Dang et al., 2017; Mattioni and Novère, 2013; Lignani et al., 2013), and properties such as cell numbers and neurite lengths can serve as cues for such changes (Kim et al., 2022; Sordini et al., 2021). For instance, blue light exposure can cause the retraction of neurites in neurons differentiated from neuroblastoma cells, resembling pathological neurite degradation, while red-light can induce the regrowth of retracted neurites (Kao et al., 2019; Chang et al., 2014). Furthermore, the direction of neurite extension provides insights into neurite outgrowth and nerve guidance (Chédotal, 2019; Endo et al., 2016). However, the analysis of phase contrast biological images is challenging due to the presence of halo and shade-off artifacts (Vicar et al., 2019), as well as the diverse shapes and sizes of neurons, making segmentation difficult (Greenwald et al., 2022). In addition, measuring the neurite length and direction of neurite extension typically involves manual tracing, which is time-consuming and may yield inconsistent

* Corresponding authors at: Max Planck Institute of Microstructure Physics, Weinberg 2, Halle D-06120, Germany.
E-mail addresses: kamydang@mpi-halle.mpg.de (K.M. Dang), joyce.poon@mpi-halle.mpg.de (J.K.S. Poon).

https://doi.org/10.1016/j.jneumeth.2024.110273
Received 2 May 2024; Received in revised form 23 June 2024; Accepted 25 August 2024
Available online 27 August 2024
0165-0270/© 2024 The Author(s). Published by Elsevier B.V. This is an open access article under the CC BY-NC license (http://creativecommons.org/licenses/by-nc/4.0/).

results in repeated measurements. To address these challenges, numerous image-processing algorithms have developed using software such as ImageJ, and toolboxes in Matlab, enabling semi-automatic or automatic detection and quantification of neuronal structures (Boulan et al., 2020; Torres-Espín et al., 2014; Pemberton et al., 2018; Kim et al., 2015; Long et al., 2017; Ho et al., 2011). The most commonly used algorithms for analyzing neuronal development are catered to fluorescence microscopy that utilize indicators to color cells and neurites. However, using fluorescent indicators can cause cellular damage or change neuronal properties (Stockley et al., 2017). Thus, depending on the application, modifying cells for fluorescence microscopy is not always possible (Alford et al., 2009; Lulevich et al., 2009).

Recently, supervised learning using deep learning has offered a solution to analyzing phase-contrast microscope images that overcomes the limitations of conventional analysis methods (Su et al., 2013). Neural networks, specifically convolutional neural networks (CNNs), have shown success in cell segmentation (Xu et al., 2019), providing more accurate segmentations with greater robustness (LeCun et al., 2015). Among CNN-based methods, U-Net has emerged as the most widely adopted approach for image segmentation, delivering promising results in live cell images (Falk et al., 2019; Ronneberger et al., 2015). However, manually creating image segmentation masks for training models is a time-intensive process, resulting in a limited number of training images (Dinsdale et al., 2022). Furthermore, deep learning approaches for quantitative biological images have mostly focused on the cell morphology (Kwonmoo Lee; Helgadottir et al., 2021), or single-cell segmentation among multiple types of cells (Stringer et al., 2021). Automated segmentation of cell in phase-contrast microscopy images using deep learning models have been introduced by Ayanzadeh et.al (Ayanzadeh et al., 2020, 2019) and Shrestha et.al (Shrestha et al., 2023). Additionally, Zhou et.al introduced DeepNeuron (Zhou et al., 2018) for tracing of axon and dendrite morphology in light microscopy images, but it lacks quantitative information about neurite length and orientation. An effective model for automated segmentation and quantification of neurites is needed in neuronal studies.

In this paper, we develop a well-tuned machine learning model for neuronal image segmentation based on a modified U-Net architecture. Additionally, we present a software package called NeuroQuantify, which offers functionalities such as cell and neurite detection, counting, neurite length measurement, and neurite orientation distribution of two dimensional (2D) images. This comprehensive tool enables quick and efficient quantitative evaluation of neuronal circuits, providing valuable insights into neuronal networks on a large scale. NeuroQuantify is implemented in Python 3 using open-source packages and is freely available for download and local installation from GitHub. Its user-friendly graphical interface facilitates precise annotation of cells and neurites from phase-contrast microscopy images, making it a useful resource for investigating biological questions concerning neuronal networks.

2. Material and methods

We introduce a neuron quantification method based on deep learning for cell and neurite segmentation. Our method uses phase-contrast microscope images and labeled images as masks to train the neural network. After image segmentation, an algorithm of image post-processing is performed for neuron quantification. Fig. 1 illustrates our computational pipeline: First, a deep learning model classifies features

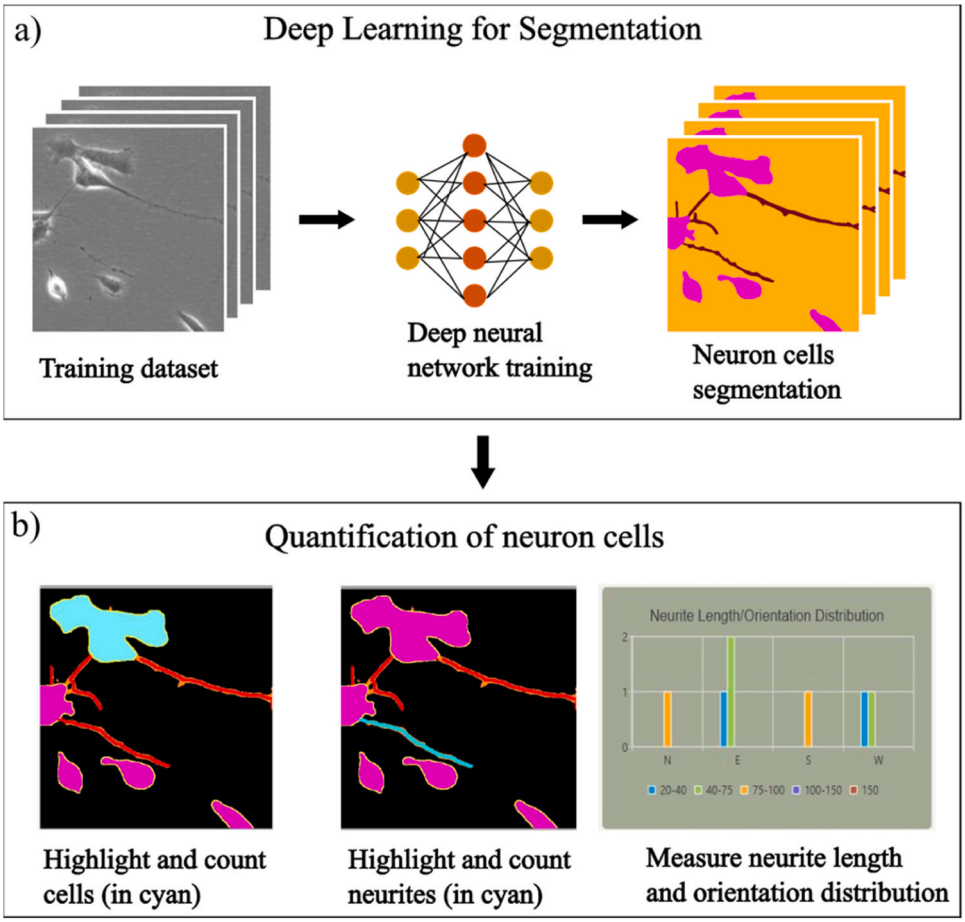

Fig. 1. Overview of the computational pipeline of NeuroQuantify, a) Deep learning for cell and neurite segmentation, and b) Quantification number of cells and measurement of neurite lengths and its orientation distribution.

in the image as cells or neurites (Fig. 1a), then the cells and neurites are counted, and the lengths and orientations of the neurites are measured (Fig. 1b).

2.1. Dataset

2.1.1. Data acquisition and preprocessing methodology

2.1.1.1. Dataset collection. The dataset and the ground truth data employed in this study encompasses two-dimensional (2D) phase-contrast microscopy images of neuroblastoma cells (SH-SY5Y). These neuron-like cells were grown in a T25 flask and treated with Retinoic acid (R2625, Sigma–Aldrich) following a standard protocol (Kovalevich and Langford, 2013). The imaging process was initiated on the third day of cultivation, using a Zeiss microscope with a 10x magnification objective and phase contrast mode. Multiple regions of interest were selected on each T25 flask, focusing on the areas with a high density of cells and neurites. Each image has a resolution of 2560×1920 pixels.

2.1.1.2. Manual annotation and class labeling. To facilitate subsequent analysis, a total of 200 images (2563×1920 pixels) were manually annotated, using a specialized software provided by ByteBridge. Three different classes on the image were assigned distinct colors corresponding to cells, neurites, and background.

2.1.1.3. Image enhancement through gamma correction. The raw phase-contrast microscope images displayed variations in background brightness levels, which could potentially introduce inconsistencies during subsequent processing. To ensure consistency in the output images, gamma correction is applied according to the following equations:

$$\gamma = \frac{\log(255 \times 0.5)}{\log(\text{mean}(\text{Input image gray values}))} \tag{1a}$$

$$\text{Output image} = (\text{Input image})^{\gamma} \tag{1b}$$

From Eq. (1a), the original image brightness value is first compared to the relative brightness parameter $\log(255 \times 0.5)$, and then the adjustment is conducted using Eq. (1b). This correction process equalizes the brightness level, reducing bias in the subsequent training process.

2.1.1.4. Image cropping and dataset generation. The initial phase-contrast images, with a size of 2563×1920 pixels, were divided into training, validation, and test sets. Each of these images was cropped into 20 smaller images each with a smaller size of 512×512 pixels (Fig. 2). During the crop, filtering was applied to remove the small images (512×512 pixels) that contained a scale bar on the corner of the image and those displaying mostly background. The 512×512 size was selected due to the memory limitation during the model training process. The final datasets consist of training dataset (2740 frames), validation set (247 frames), and test set A (323 frames), where the size of each frame was 512×512 pixels. To accurately assess cellular and neurite counts, as well as neurite lengths within the high-resolution images (2563×1920 pixels), an additional test set of 20 images with 2563×1920 pixels was deliberately introduced. The test set images (ground truth) were chosen with cell densities varying from 1 % to >10 % and captured in various experiments. Cell density is defined by the fractional area of the image occupied by the cell body. This supplementary dataset, called test set B, served the explicit purpose of evaluating the performance of the post-processing phase, i.e. the analysis of the segmentation masks, and has not been used during the training of the neural network. The segmentation mask of these high-resolution images has been enriched by information on the number of cells and neurites manually counted by an expert using ImageJ, and the average length of the neurites as given by the NeuronJ plugin.

2.2. Neural network architecture

2.2.1. U-net for semantic segmentation

The models used in the paper are based on U-Net, which consists of an encoder and a decoder. U-Net is a CNN specifically designed for biomedical image segmentation. Its architecture includes a contracting path to capture context and an expanding path for precise localization. The model generates a pixel-by-pixel mask that represents the class of each pixel. One major advantage of the U-Net model is its ability to learn effectively from a relatively small dataset.

Fig. 3 illustrates the architecture diagram for the primary model used in our work, referred to as the large model. This model consists of 4 down-sampling blocks and 4 up-sampling blocks, with an initial convolutional block with 64 output channels. In each down-sampling block, the input data undergoes two consecutive 3×3 kernel size convolutions with a ReLu activation function. Subsequently, a 2×2 kernel max pool layer is applied to reduce data size. After the fourth block, the data enters the up-sampling path. During up-sampling, the data undergoes a reverse convolution layer with a 2×2 kernel and half the original number of features. It is then concatenated with a copy of the data outputted at the same block level in the down-sampling path. The combined tensor is passed through a double convolution layer, with the number of output channels matching the reverse convolution step. Finally, after 4 blocks of up-sampling, the data goes through a 3×3 convolutional layer with an output channel size set of 3, performing the final three-class segmentation task. In addition to the large model, there is also a simplified model, named small model. This model comprises 3 blocks of down-sampling and 3 blocks of up-sampling. The number of output channels in the initial convolution block is reduced to 16 features, significantly reducing the random access memory usage during training. The small model demonstrates more efficient computation in practice.

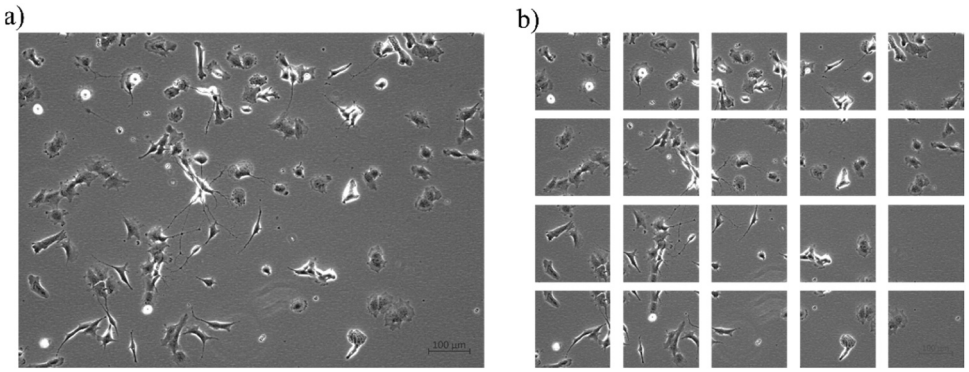

Fig. 2. a) An original image, size of 2653×1920, and b) 20 smaller images of size 512×512 retrieved from the same image.

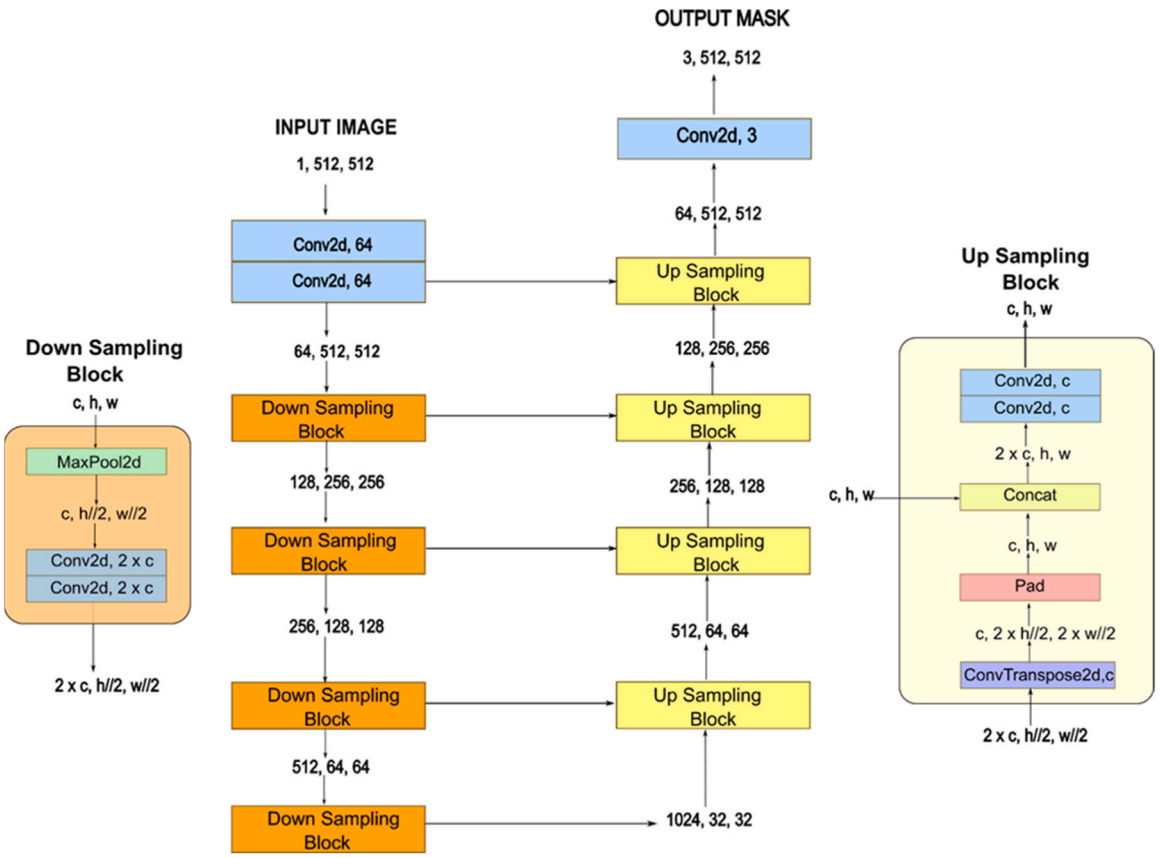

Fig. 3. U-Net architecture in NeuroQuantify (large model). The large model uses 4 down sampling blocks and 4 up sampling blocks, while only 3 of each are used for small model. Both models use ReLU as activation functions. Down Sampling blocks extract and transform features, simultaneously reducing the spatial dimensions. Up sampling block restore spatial dimensions for improved localization. In the diagram, the shape of the tensors is also shown in channel-first format (c, h, w representing channels, the height and the width of a tensor).

2.2.1.1. Training process. The models have been trained on the 2740 512×512 frames in the training dataset. For both the large and small models, we used the Adam optimizer with a learning rate of 0.0001. The Adam optimizer (Adaptive Moment Estimation) is an iterative optimization algorithm used to minimize the loss function during the training of neural network (Kingma and Ba, 2017). It adjusts the learning rate for each parameter and to achieve fast convergence and reliable performance. The learning rate, as well as hyper-parameters, was selected through a process of optimization, driven by the generalization performance of our models evaluated on the 247 images in the validation set.

2.2.1.2. Loss function. We used a combination of cross entropy loss (CE) (CoinCheung, 2023) and soft dice loss (CrossEntropyLoss) as the loss function to train both the small and large model. CE is widely used for classification tasks, and it measures the dissimilarity between the predicted probability distribution and the ground truth label for each pixel. To emphasize the segmentation performance for the cells and neurites while minimizing the impact on the background pixels, rescaling weight were assigned to each class when computing the overall CE. Specifically, the weight factor was set to 2.0 for background, 3.0 for cell bodies, and 5.0 for neurites.

The D function is computed individually for each class separately and then averaged to obtain a final score (An overview of semantic image segmentation, 2018). Using soft dice loss, the model mitigates the issue of inflated accuracy caused by correctly classifying the background, which takes most of the region within the image. Instead, it prioritizes the accuracy of cell classification by assessing intersectional aspects.

The global loss functions of the large and small models are, respectively,

$$L_{large} = 0.5D + 0.5CE, \tag{2a}$$

$$L_{small} = 0.8D + 0.2C. \tag{2b}$$

2.3. Image post processing

2.3.1. Algorithm for cell counting and neurites analysis from segmentation mask

After performing image segmentation, we proceeded to group non-adjacent cells into cell clusters, while non-adjacent neurites were grouped into clusters based on their connections. Subsequently, we assigned the corresponding neurite groups to their respective cell clusters. To perform precise measurement of neurite length, we considered neurites originating from cells within the image to identify both the original spot where the neurite begins to grow and its endpoint, while excluding those originating from cells outside the image.

To count the number of cells, we started by establishing a typical area based on the histogram of cell area distribution on 200 images of our training dataset (Figure S1). We observed that the distribution centered around approximately 40 μm in diameter, with the corresponding cell area of approximately1256 μm^2. For each cell cluster, we calculated the number of cells by dividing the cluster area by the typical cell area and rounding to the nearest integer. Adding the number of cells across all clusters yielded the final cell count for the image.

To determine the number of neurites and analyze their length, we based on the segmentation mask. The segmentation mask categorizes each pixel as background, cells or neurites accordingly. Fig. 4a shows the segmentation mask with three colors for background, cells and neurites. The masked pixels for the cells and neurites are then filtered

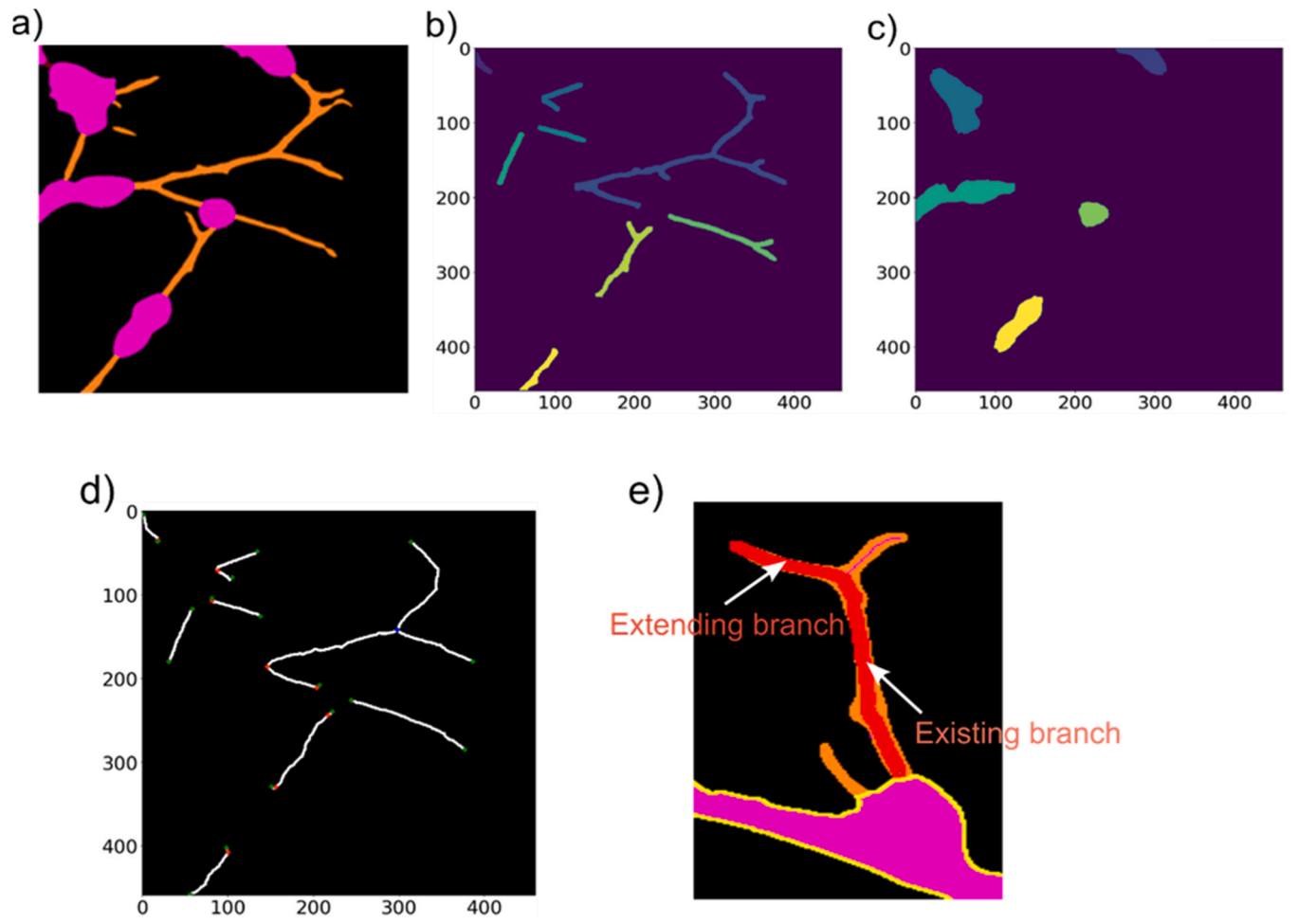

Fig. 4. Post-image processing for neurite length quantification a) segmentation of prediction image, b) filtered image of neurites, c) filtered image of cells with different colors, d) neurite skeleton, e) priority of adding an extending branch into an existing branch.

out separately by colors as shown in Fig. 4b and c. To convert the segmentation neurite region to a single-pixel-width skeleton along the center region, we used skeletonization in the fil-finder library (Koch and Rosolowsky, 2015), resulting in the neurite skeleton shown in Fig. 4d. In this figure, white lines represent the neurite skeleton, green dots indicate "end points"; blue dots signify "intersection points", and red dots denote "touch points". The presence of "touch points" aims to include the connectivity of the neurites and cells in the analysis. They are the closest points on the skeleton where the neurite and the cell are connected. The "touch points", "intersection points" and "end points" separate the neurites into smaller branch segments and do further analysis. After the detection of neurites, NeuroQuantify measures the length and orientation of the detected neurites. The length of a neurite is calculated based on the scale information of captured images (1 μm = 2.21 pixel). In scope of our analysis, we only count neurites with lengths longer than 20 μm to eliminate short neurites that are potential noise from the segmentation mask. In case where multiple neurites protrude from a single location in the cluster, we only count the longest. When the neurites cross each other, we trace their origins. Therefore, the algorithm is designed to find a "touching" branch segment which starts from at least one "touch point" and use it as the starting of a branch. Then we assign additional branch segments that are directly connected to the previous branch. This process is repeated until no branch segment can be found. In case there are multiple branches connected to the previous branch, the program counts the extending branch with the longer projection length on the existing branch. The longer projection branch is illustrated as Fig. 4e. By applying these criteria, the data can be effectively analyzed and processed to obtain meaningful insights.

2.4. Evaluation metrics

2.4.1. Metrics for semantic segmentation: precision, Recall, F1 score, IoU score

To evaluate the performance of our deep learning models, we computed the metrics including total precision, per-class recall, and F1 score. The metrics are defined as follows,

$$\text{Total Precision} = \frac{TP_{cell} + TP_{neurite} + TP_{background}}{TP_{cell} + TP_{axon} + TP_{bg} + FP_{cell} + FP_{neurite} + FP_{background}} \tag{3a}$$

$$\text{Recall} = \frac{TP}{TP + FN} \tag{3b}$$

$$\text{F1 score} = \frac{2 \times \text{Precision} \times \text{Recall}}{\text{Precision} + \text{Recall}} \tag{3c}$$

where TP, FP, and FN are respectively per class true positive, false positive, false negative. The detailed definition of TP, FP and FN for multi-classification can be seen in the supplementary.

The intersection over union (IoU) score is computed to estimate how well the segmentation of each class matches the ground truth mask at the pixel level. The IoU score is given by

$$IoU = \frac{A \cap B}{A \cup B} \tag{3d}$$

where A is a predicted class and B is the corresponding ground truth mask.

2.4.2. Metrics for cell, neurite counting and average neurite length accuracy

The accuracy is calculated by comparing the predicted cell, neurite count and average neurite length from the predicted segmentation images analyzed by NeuroQuantify with the ground truth images. The

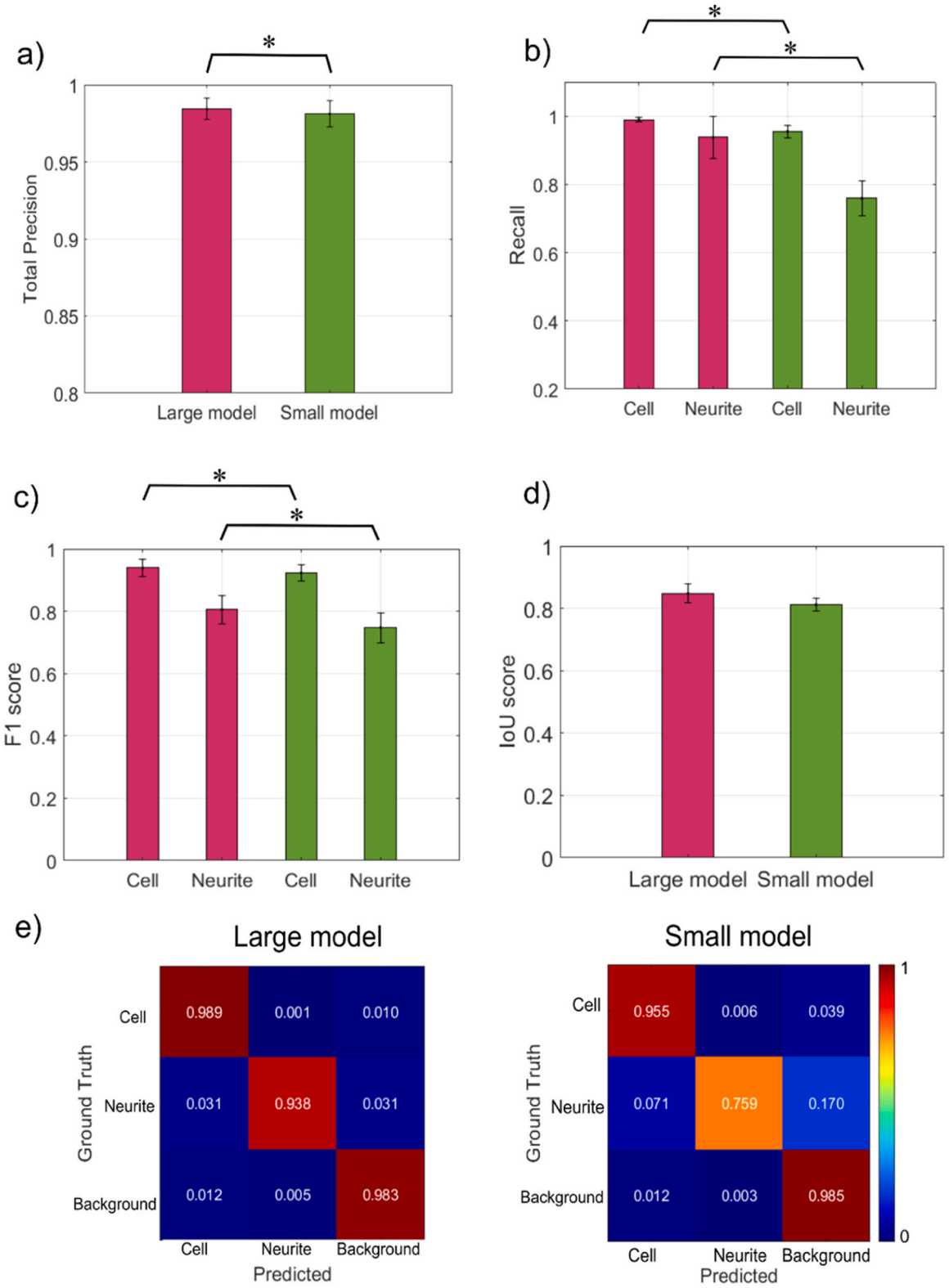

Fig. 5. Comparison of performance for two models in NeuroQuantify. Significance was tested by the two-sided Wilcoxon signed-rank test, (*): $p < 0.05$; The bar plots shows the average and the standard deviation across the images in test set A of a) the total precision; b) the cell and neurite recall; c) the cell and neurite F1 score, d) the IoU score, and e) confusion matrices of the segmentation performance for the large and small models.

equation used is as follow:

$$\text{Accuracy} = 1 - \frac{|\text{Predicted} - \text{Ground Truth}|}{\text{Ground Truth}}. \quad (4)$$

3. Results

In the sections to follow, we summarize the results of the model. We begin by evaluating the large and small models in the segmentation task using the test set A in Section 3.1. In Section 3.2, we present the analysis pipeline including the post processing phase. We discuss the accuracy in the cells and neurites counting tasks by comparing the prediction of NeuroQuantify with the annotations by experts, and the neurite length measurement using NeuroQuantify is compared with the NeuronJ plugin from ImageJ. In Section 3.3, we highlight the advantages of our post-image processing, including cell counting with neurites, neurite orientation distribution. Finally, Section 3.4 introduces a user-friendly graphical interface and provides information regarding its processing time for two models.

3.1. Validating the segmentation performance in the large and small model

We evaluated the performances in the segmentation task of two deep learning models using the images of neuroblastoma cells contained in test set A. As discussed in Section 2.4, to quantitatively evaluate the quality of a segmentation mask we used the total precision, the per-class recall, F1 score, and the IoU score (Eqs. (3a), (3b), (3c), and (3d)).

To assess the statistical significance of performance between the two models, we employed the two-sided Wilcoxon signed-rank test with a significance level of 0.05. Fig. 5 shows the results. The average total precision for three classes segmentation in both models is significantly high, reaching approximately 0.98. Fig. 5b shows that the large model exhibits significant higher average recall values for cells and neurites compared to the small model (0.98 vs. 0.93 for cells, and 0.95 vs. 0.75 for neurites), suggesting that the large model more effectively detects cells and neurites. There is significant difference in the F1 score for the cell and neurite class between two models as shown in Fig. 5c.

To further evaluate the precision of object detection in both models, we used IoU score, which measures the overlap between the predicted image and the ground truth mask. Fig. 5d illustrates the result. Both models attain a high IoU matching, with the large model achieving an IoU score of 0.84, while the small model achieves a score of 0.81. Fig. 5e presents the confusion matrices for both the large and small models, highlighting the improved accuracy in cells and especially the neurites detection achieved by the large model.

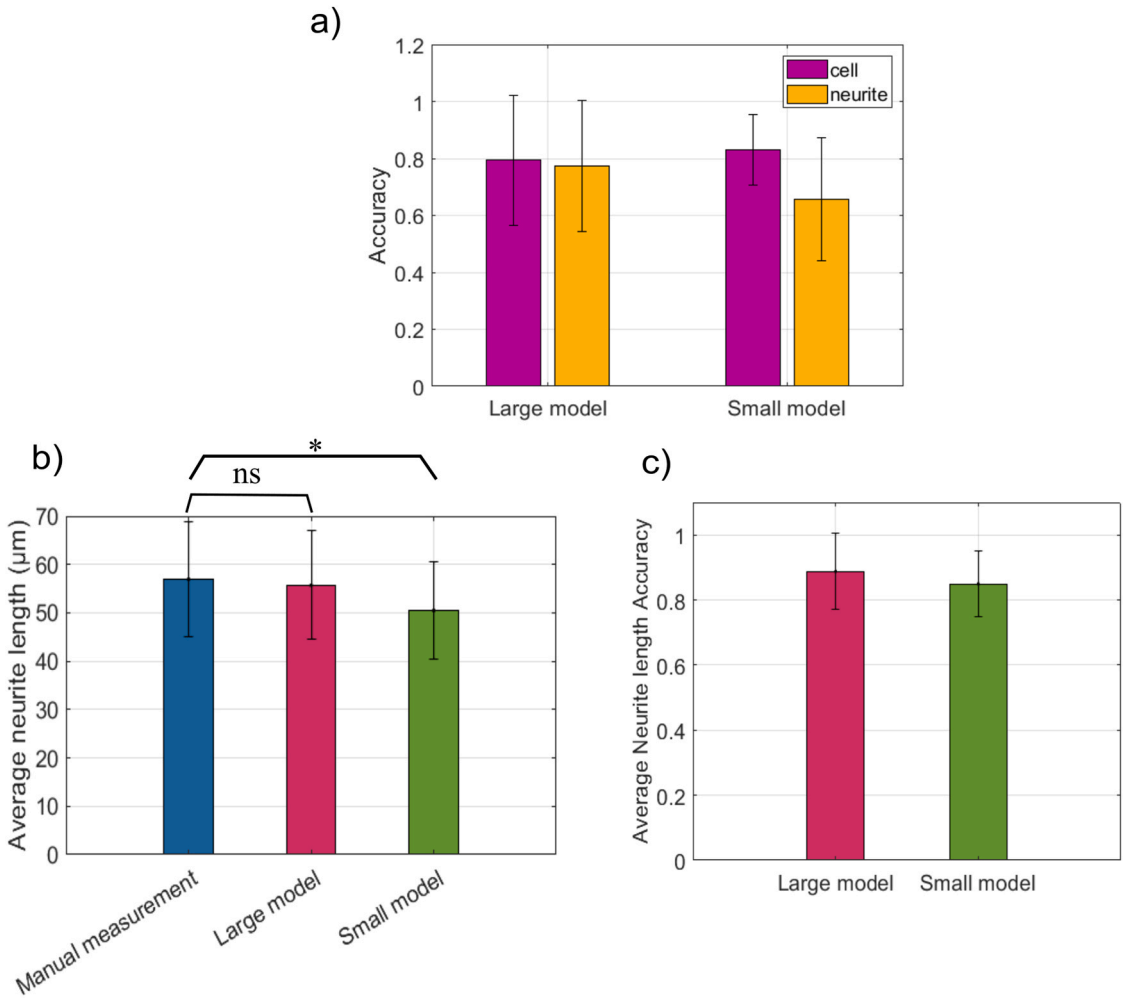

Fig. 6. Evaluation of the segmentation performance of NeuroQuantify in the small and large models by calculating the accuracy of number of cells, neurites and neurite length quantification, Significance was tested by the two-sided Wilcoxon signed-rank test, ns: $p > 0.05$; *: $p < 0.05$; a) the accuracy of the number of cells and number of neurites as predicted by both models, b) a comparison between manual measurement and automated measurement using the large and small models, and c) a plot of average and standard deviation of neurite length accuracy for both models.

3.2. Assessing cell and neurite count accuracy with NeuroQuantify

3.2.1. Accuracy of cell and neurite counting using NeuroQuantify

We used test set B consisting of 20 high-resolution phase-contrast images (2563×1920 pixels) to assess the capabilities of NeuroQuantify in counting cells and neurites by comparing the predicted images from NeuroQuantify with the ground truth. In Fig. 6a, we present the accuracy of cell and neurite classification. Interestingly, the small model exhibits slightly higher accuracy in cell prediction compared to the large model. Specifically, the small model achieves an accuracy of 0.83, while the large model achieves 0.79. Regarding neurite detection, the small model achieves 0.65 accuracy, while the large model achieves 0.77.

We examined the inaccurate segmentation of the small model for neurite detection by investigating the predicted masks (segmented image from the model), where neurites are colored in orange, and the skeleton masks (image after post-processing), where neurites are colored in red. As shown in Figure S3a-d, which provides examples of neurite detection, both the large and small models exhibited a similar ability to detect long neurites (with lengths > 20 μm). However, when using the skeleton mask for neurite counting, the small model tended to overlook short neurites (with lengths < 20 μm). This issue is further illustrated in Figure S3e-g, where the small model failed to detect the short neurites.

3.2.2. Accuracy of neurite length quantification using NeuroQuantify

A feature of NeuroQuantify is the quantification of the neurite length. To assess the effectiveness of NeuroQuantify in measuring neurite lengths, we compared the average results on test set B with the ground truth obtained by NeuronJ, an ImageJ plugin (NeuronJ, ImageJ Wiki). To determine the statistical significance between the two methods, we conducted a two-sided Wilcoxon signed-rank test at a significance level of 0.05. Fig. 6b illustrates the comparison of average neurite length measurements between NeuroQuantify and manual

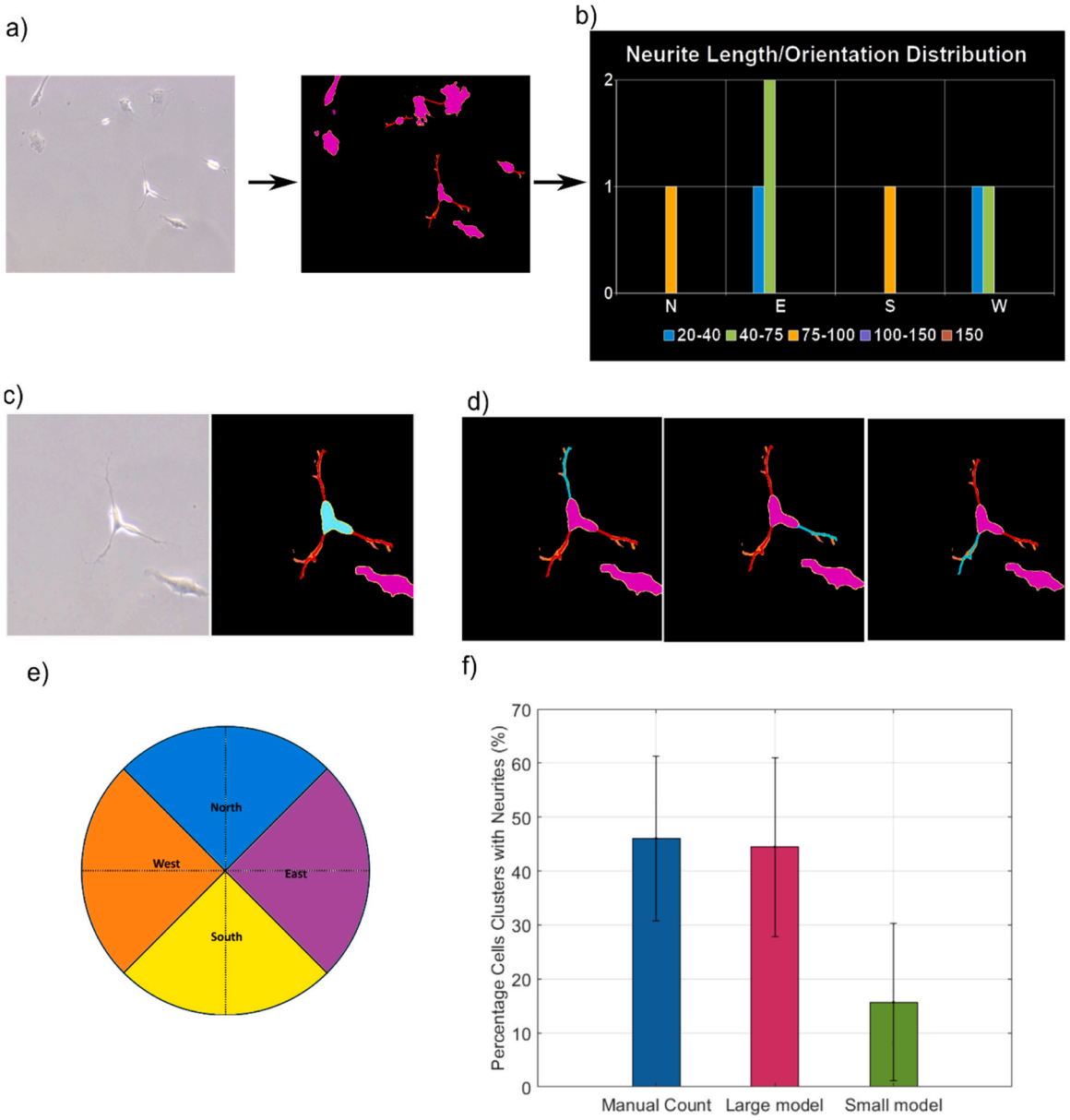

Fig. 7. Post-processing of the images for analyzing neurite orientation distribution. a) an example of image post-processing from the phase-contrast image input to annotation mask and b) a plot of neurite length and neurite orientation distribution of the whole image, the color bars indicate the range of neurite length, the number of neurites presented on y-axis and the orientation of neurites presented on x-axis, c), d) show an example of neurite orientation distribution (N, E, S from left to right respectively), e) a diagram shows definition of neurite orientation in NeuroQuantify, and f) Percentage of cell clusters with neurite counted manually and using the large and small models.

measurement. The results reveal that there is no significant difference between the manual technique and the large model ($p > 0.05$), whereas the small model exhibits a significant difference in neurite length measurement ($p < 0.05$). Furthermore, Fig. 6c presents a plot illustrating the average neurite length accuracy for test set B. As depicted in Fig. 6c, the average neurite length accuracy of both models is quite similar, with a value of 0.88 for the large model, and 0.84 for the small model.

3.3. Neurites orientation distributions and counting cells with neurites using NeuroQuantify

NeuroQuantify offers an additional feature of providing the orientation distribution of neurites in the images. The orientation of a neurite is determined by drawing a straight line from the point where it attaches to the cell (known as the touch point) to its endpoint. If the other end of the neurite is connected to another cell, the orientation will be displayed in both directions. Four directions, namely north (N), south (S), east (E), and west (W), are defined to represent the neurite orientation (Fig. 7e). NeuroQuantify allows users visualize the orientation of individual neurites which belong to a specific cell (Figure S4). Fig. 7a and b illustrate the post-image processing steps involved in analyzing the neurite orientation. Fig. 7c and d provide an example of a single cell with three neurites, each pointing in a different direction.

Furthermore, NeuroQuantify offers the capability to count the number of cells that have neurites. The algorithm specifically counts cells with neurites attached to it based on an adjacency analysis of the skeleton mask. The comparison of the manual counting and performance of the NeuroQuantify models in terms of the average percentage of cells with neurites is shown in Fig. 7**f**. As shown in the figure, the small model was less effective in recognizing neurites when connected to cell clusters. Conversely, the large model demonstrates a similar percentage of cell clusters with neurites compared to manual counting.

3.4. NeuroQuantify user interface and processing time

To make the NeuroQuantify easier to use, we have developed a graphical user interface, as shown in Fig. 8a. The user interface utilizes the Python library PyQt6 as its primary framework. This choice of

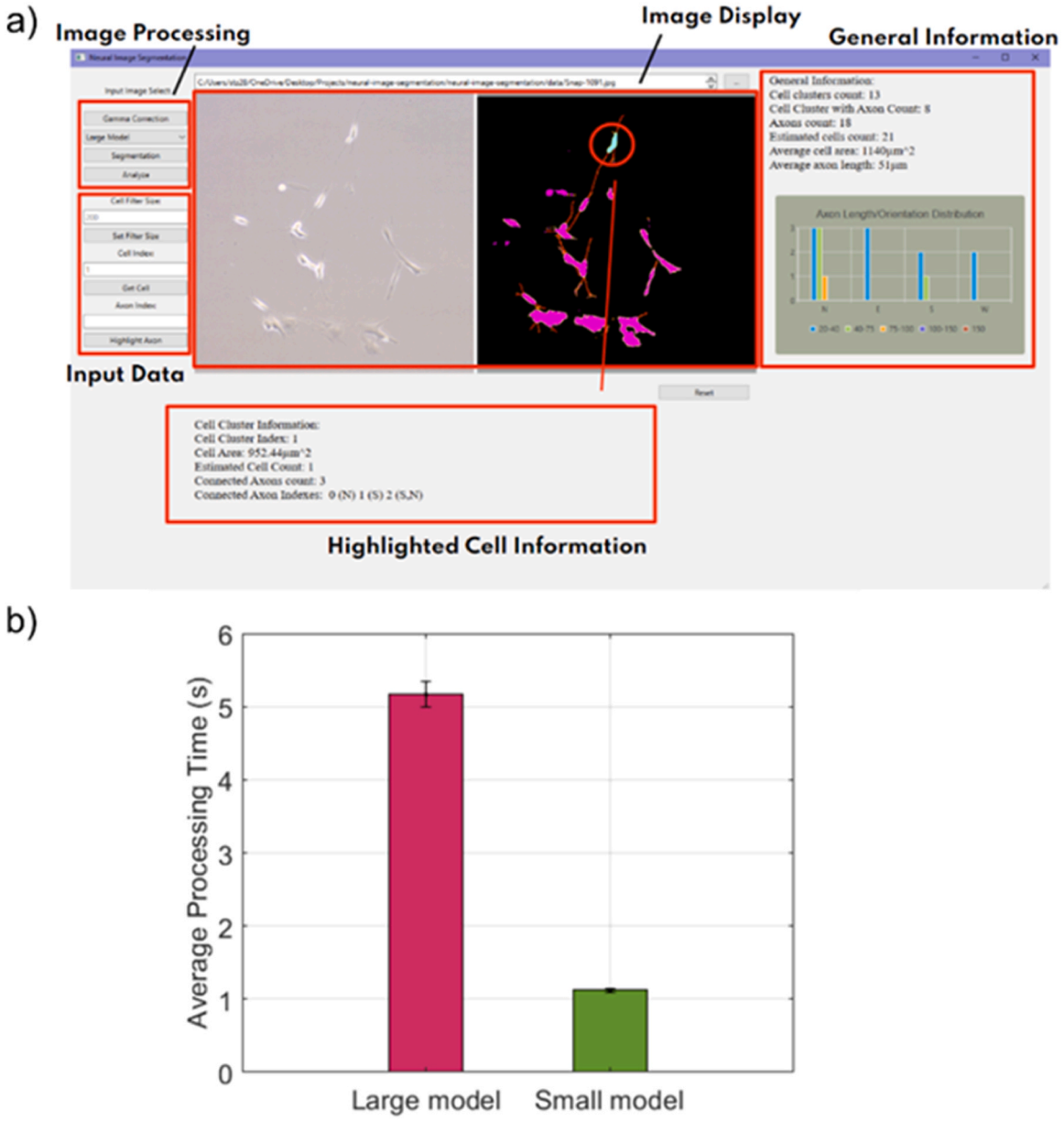

Fig. 8. a) User Interface of NeuroQuantify and b) a comparison of the average processing time of the large and small models of NeuroQuantify.

framework ensures cross-platform compatibility, enabling users to access NeuroQuantify seamlessly on Windows 10 (1809 or later), MAC OS (12/11/10.15) (64 bit Intel, 64 bit ARM; XCode 12), and Linux (Ubuntu 20.04 (64 bit Intel; gcc9), CentOS Linux 8.2, SLES 15 SP2 (SUSE Linux Enterprise Server, 64 bit Intel; gcc10), Open SUSE 15.3 (64 bit; gcc9)). Additionally, since the main algorithm and machine learning model have been implemented in Python, the integration of PyQt6 provides a more streamlined connection for Python-based functionalities. Within this user interface, as illustrated in Fig. 8a, users can interact with NeuroQuantify by simply clicking on cells or neurites of interest. Upon selection, NeuroQuantify highlights the selected elements and provides relevant information. Moreover, users have the option to export neurite length information as a csv file, while the generated plot depicting neurite orientation and annotated data is automatically saved in the result folder. The analysis of neurite orientation offers valuable insights for studying axon guidance in diverse local environments (Matsumoto et al., 2021; Andersson et al., 2020).

To assess the performance of NeuroQuantify, we compared the processing time between two models using 20 images in the test set B. The processing time encompasses segmentation, annotation and post-image processing, which involves tasks such as cell and neurite counting, neurite length measurement, and neurite orientation distribution analysis. This analysis was conducted on a laptop with an 11th generation Intel i7–11800 H CPU, 16 GB of RAM, Windows 10. Fig. 8b presents the processing time for both models. As depicted in Fig. 8b, the processing time for the large model is approximately five times longer than that of the small model.

4. Discussion

We have introduced a comprehensive framework for neuron detection and semantic segmentation in images of neuron-like neuroblastoma cells. Automatic quantification of phase-contrast neuron culture images can accelerate laboratory investigations, and neurites are studied in the context of neuron regeneration and neurodegenerative diseases (Wu et al., 1998; Szarowicz et al., 2022; Hussain et al., 2018; Costa et al., 2022). Neuroblastoma cells share certain characteristics with primary neurons, particularly in their highly elaborate axon structures, which make them suitable for *in vitro* studies simulating primary neuron attachment and proliferation (Arslantunali et al., 2014). These cells are commonly employed in research on neurodegeneration and neuro-regeneration diseases (Shea et al., 1991; Su et al., 2017; Hoffmann et al., 2022; Bell and Zempel, 2022). The NeuroQuantify models offer precise analysis of neurite structures, including measurements of neurite length and the distribution of orientations. The models allow users to analyze complex neuronal networks within seconds. Importantly, our large model achieves performance levels comparable to those of human experts. Figure S5 illustrates a comparison between a phase-contrast image and a segmented image generated by NeuroQuantify. High-quality images are crucial for achieving accurate results. Our observation of the ground truth images indicate that the model's accuracy depends highly on image quality. We analyzed our data to access accuracy across various cell density levels. As shown in the Figure S6, cell density does not significantly affect the model's accuracy. The figure shows that the accuracy is lower for the low-density images compared to high-density cell images. The discrepancy is due to the lower contrast in the low-density cell images.

Despite the promising segmentation results, certain aspects of our algorithms can be improved. Firstly, it is necessary to enhance the accuracy of neurite detection (shorter than 20 μm) in the small model. This can be achieved by conducting additional training with a larger dataset with higher magnification, which would contribute to higher accuracy. Techniques like data augmentation can be employed to introduce more variations in the existing dataset during model training. Additionally, conducting further experimentation with hyperparameter tuning for different model parameters can help identify the most optimal configuration. Secondly, a limitation of our models is that the U-Net model has been trained specially using our dataset with the 10x microscope images. As such, its performance for segmenting images captured with different types of microscopes or at varying magnification remains unverified. To make NeuroQuantify more universally applicable in diverse capture environments, it is imperative to gather additional datasets encompassing various imaging conditions.

While our primary objective has been to develop an algorithm for quick and efficient analysis of neuronal networks in neuroblastoma cells, NeuroQuantify also offers the possibility to analyze other cell types, such as PC12 cells (as depicted in Figure S7). Overall, NeuroQuantify demonstrates its potential for quantitatively assessing neuron cells and their associated networks. It exhibits a high level of effectiveness in segmenting cells and neurites within intricate structures, while also providing accurate quantitative measurements of their length and orientations.

5. Conclusion

In summary, we have introduced NeuroQuantify, a deep learning model for detecting and segmenting cells and neurites in phase contrast microscopy 2D images, without the need for fluorescence labelling. NeuroQuantify can analyze the images within a few seconds to provide quantitative information about cell numbers, neurite numbers, neurite lengths, and neurite orientation distribution. These functionalities are useful for biological research requiring assessments of neuronal network development. Potential extensions to this work are to implement and evaluate NeuroQuantify's performance in three-dimensional (3D) images, to be able to infer 3D information from 2D images, and to improve the neurite detection accuracy.

CRediT authorship contribution statement

Chao Wang: Writing – review & editing, Writing – original draft, Validation, Software, Methodology. **Tianchen Zhang:** Writing – review & editing, Writing – original draft, Validation, Software, Methodology, Formal analysis. **Anton Sinner:** Validation, Methodology, Investigation, Formal analysis, Data curation. **Yi Jia Zhang:** Writing – review & editing, Writing – original draft, Validation, Software, Methodology, Formal analysis. **Ka My Dang:** Writing – review & editing, Writing – original draft, Supervision, Methodology, Formal analysis, Data curation, Conceptualization. **Joyce Poon:** Writing – review & editing, Writing – original draft, Supervision, Project administration, Funding acquisition, Conceptualization. **Piero Coronica:** Writing – review & editing, Writing – original draft, Supervision, Software, Methodology.

Declaration of Competing Interest

The authors declare no conflict of interest.

Data Availability

The code and data are publicly available.

Acknowledgments

The authors would like to thank Prof. Dr. Tome Kosteski from University of Toronto, Dr. Andreas Marek from Max Planck Computing and Data Facility, and Dr. Michael G. K. Brunk from Max Planck of Microstructure Physics for helpful discussions. This work was supported by the Max Planck Society.

Appendix A. Supporting information

Supplementary data associated with this article can be found in the online version at doi:10.1016/j.jneumeth.2024.110273.

References

Alford, R., Simpson, H.M., Duberman, J., Hill, G.C., Ogawa, M., Regino, C., Kobayashi, H., Choyke, P.L., 2009. Toxicity of organic fluorophores used in molecular imaging: literature review. Mol. Imaging 8, 341–354.

An overview of semantic image segmentation., Jeremy Jordan (2018). ⟨https://www.jeremyjordan.me/semantic-segmentation/⟩ (Accessed June 14, 2023).

Andersson, M., Kjer, H.M., Rafael-Patino, J., Pacureanu, A., Pakkenberg, B., Thiran, J.-P., Ptito, M., Bech, M., Bjorholm Dahl, A., Andersen Dahl, V., Dyrby, T.B., 2020. Axon morphology is modulated by the local environment and impacts the noninvasive investigation of its structure–function relationship. Proc. Natl. Acad. Sci. 117, 33649–33659. https://doi.org/10.1073/pnas.2012533117.

Arslantunali, D., Budak, G., Hasirci, V., 2014. Multiwalled CNT-pHEMA composite conduit for peripheral nerve repair. J. Biomed. Mater. Res. A 102, 828–841. https://doi.org/10.1002/jbm.a.34727.

Ayanzadeh, A., Ozuysal, O.Y., Okvur, D.P., Onal, S., Tgreyin, B.U., Unay, D., 2020. Deep Learning based Segmentation Pipeline for Label-Free Phase-Contrast Microscopy Images. 2020 28th Signal Process. Commun. Appl. Conf. SIU. IEEE, Gaziantep, Turkey, pp. 1–4. https://doi.org/10.1109/SIU49456.2020.9302304.

Ayanzadeh, A., Yağar, H.O., Özuysal, Ö.Y., Okvur, D.P., Töreyin, B.U., Ünay, D., Önal, S., 2019. Cell Segmentation of 2D Phase-Contrast Microscopy Images with Deep Learning Method. 2019 Med. Technol. Congr. TIPTEKNO, pp. 1–4. https://doi.org/10.1109/TIPTEKNO.2019.8894978.

Bell, M., Zempel, H., 2022. SH-SY5Y-derived neurons: a human neuronal model system for investigating TAU sorting and neuronal subtype-specific TAU vulnerability. Rev. Neurosci. 33, 1–15. https://doi.org/10.1515/revneuro-2020-0152.

Boulan, B., Beghin, A., Ravanello, C., Deloulme, J.-C., Gory-Fauré, S., Andrieux, A., Brocard, J., Denarier, E., 2020. AutoNeuriteJ: An ImageJ plugin for measurement and classification of neuritic extensions. PLOS ONE 15, e0234529. https://doi.org/10.1371/journal.pone.0234529.

Chang, K.-Y., Woo, D., Jung, H., Lee, S., Kim, S., Won, J., Kyung, T., Park, H., Kim, N., Yang, H.W., Park, J.-Y., Hwang, E.M., Kim, D., Do Heo, W., 2014. Light-inducible receptor tyrosine kinases that regulate neurotrophin signalling. Nat. Commun. 5, 4057. https://doi.org/10.1038/ncomms5057.

Chédotal, A., 2019. Roles of axon guidance molecules in neuronal wiring in the developing spinal cord. Nat. Rev. Neurosci. 20, 380–396. https://doi.org/10.1038/s41583-019-0168-7.

CoinCheung, pytorch-loss, (2023). ⟨https://github.com/CoinCheung/pytorch-loss⟩ (accessed June 13, 2023).

Costa, G., Ribeiro, F.F., Sebastião, A.M., Muir, E.M., Vaz, S.H., 2022. Bridging the gap of axonal regeneration in the central nervous system: a state of the art review on central axonal regeneration. Front. Neurosci. 16. ⟨https://www.frontiersin.org/articles/10.3389/fnins.2022.1003145⟩ (accessed June 21, 2023).

CrossEntropyLoss — PyTorch 2.0 documentation, (n.d.). ⟨https://pytorch.org/docs/stable/generated/torch.nn.CrossEntropyLoss.html⟩ (accessed June 13, 2023).

Dang, K.M., Rinklin, P., Schnitker, J., Haberkorn, B., Zobel, K., Gribaudo, S., Perrier, A. L., Carolus, J., Daenen, M., Weigel, S., Luksch, H., Offenhäusser, A., Wolfrum, B., 2017. Fabrication of precisely aligned microwire and microchannel structures: toward heat stimulation of guided neurites in neuronal cultures. Phys. Status Solidi A 214, 1600729. https://doi.org/10.1002/pssa.201600729.

Dinsdale, N.K., Jenkinson, M., Namburete, A.I.L., 2022. STAMP: simultaneous training and model pruning for low data regimes in medical image segmentation. Med. Image Anal. 81, 102583 https://doi.org/10.1016/j.media.2022.102583.

Dravid, A., Raos, B., Svirskis, D., O'Carroll, S.J., 2021. Optimised techniques for high-throughput screening of differentiated SH-SY5Y cells and application for neurite outgrowth assays. Sci. Rep. 11, 23935 https://doi.org/10.1038/s41598-021-03442-1.

Endo, M., Hattori, M., Toriyabe, H., Ohno, H., Kamiguchi, H., Iino, Y., Ozawa, T., 2016. Optogenetic activation of axon guidance receptors controls direction of neurite outgrowth. Sci. Rep. 6, 23976 https://doi.org/10.1038/srep23976.

Falk, T., Mai, D., Bensch, R., Çiçek, Ö., Abdulkadir, A., Marrakchi, Y., Böhm, A., Deubner, J., Jäckel, Z., Seiwald, K., Dovzhenko, A., Tietz, O., Dal Bosco, C., Walsh, S., Saltukoglu, D., Tay, T.L., Prinz, M., Palme, K., Simons, M., Diester, I., Brox, T., Ronneberger, O., 2019. U-Net: deep learning for cell counting, detection, and morphometry. Nat. Methods 16, 67–70. https://doi.org/10.1038/s41592-018-0261-2.

Graves, C.E., McAllister, R.G., Rosoff, W.J., Urbach, J.S., 2009. Optical neuronal guidance in three-dimensional matrices, 10.1016/j.jneumeth.2009.02.004 J. Neurosci. Methods 179. https://doi.org/10.1016/j.jneumeth.2009.02.004.

Greenwald, N.F., Miller, G., Moen, E., Kong, A., Kagel, A., Dougherty, T., Fullaway, C.C., McIntosh, B.J., Leow, K.X., Schwartz, M.S., Pavelchek, C., Cui, S., Camplisson, I., Bar-Tal, O., Singh, J., Fong, M., Chaudhry, G., Abraham, Z., Moseley, J., Warshawsky, S., Soon, E., Greenbaum, S., Risom, T., Hollmann, T., Bendall, S.C., Keren, L., Graf, W., Angelo, M., Van Valen, D., 2022. Whole-cell segmentation of tissue images with human-level performance using large-scale data annotation and deep learning. Nat. Biotechnol. 40, 555–565. https://doi.org/10.1038/s41587-021-01094-0.

Helgadottir, S., Midtvedt, B., Pineda, J., Sabirsh, A., B. Adiels, C., Romeo, S., Midtvedt, D., Volpe, G., 2021. Extracting quantitative biological information from bright-field cell images using deep learning. Biophys. Rev. 2, 031401 https://doi.org/10.1063/5.0044782.

Ho, S.-Y., Chao, C.-Y., Huang, H.-L., Chiu, T.-W., Charoenkwan, P., Hwang, E., 2011. NeurphologyJ: an automatic neuronal morphology quantification method and its application in pharmacological discovery. BMC Bioinforma. 12, 230. https://doi.org/10.1186/1471-2105-12-230.

Hoffmann, L.F., Martins, A., Majolo, F., Contini, V., Laufer, S., Goettert, M.I., 2022. Neural regeneration research model to be explored: SH-SY5Y human neuroblastoma cells. Neural Regen. Res. 18, 1265–1266. https://doi.org/10.4103/1673-5374.358621.

Hussain, R., Zubair, H., Pursell, S., Shahab, M., 2018. Neurodegenerative diseases: regenerative mechanisms and novel therapeutic approaches. Brain Sci. 8, 177. https://doi.org/10.3390/brainsci8090177.

Kao, Y.-C., Liao, Y.-C., Cheng, P.-L., Lee, C.-H., 2019. Neurite regrowth stimulation by a red-light spot focused on the neuronal cell soma following blue light-induced retraction. Sci. Rep. 9, 18210 https://doi.org/10.1038/s41598-019-54687-w.

Kim, T., Kadji, H., Whalen, A.J., Ashourvan, A., Freeman, E., Fried, S.I., Tadigadapa, S., Schiff, S.J., 2022. Thermal effects on neurons during stimulation of the brain. J. Neural Eng. 19, 056029 https://doi.org/10.1088/1741-2552/ac9339.

Kim, K.-M., Son, K., Palmore, G.T.R., 2015. Neuron image analyzer: automated and accurate extraction of neuronal data from low quality images. Sci. Rep. 5, 17062 https://doi.org/10.1038/srep17062.

D.P. Kingma, J. Ba, Adam: A Method for Stochastic Optimization, (2017). https://doi.org/10.48550/arXiv.1412.6980.

Koch, E.W., Rosolowsky, E.W., 2015. Filament identification through mathematical morphology. Mon. Not. R. Astron. Soc. 452, 3435–3450. https://doi.org/10.1093/mnras/stv1521.

Kovalevich, J., Langford, D., 2013. Considerations for the Use of SH-SY5Y neuroblastoma cells in neurobiology. Methods Mol. Biol. Clifton NJ 1078, 9–21. https://doi.org/10.1007/978-1-62703-640-5_2.

J.J. Kwonmoo Lee, A deep learning-based segmentation pipeline for profiling cellular morphodynamics using multiple types of live cell microscopy, Cell Rep Methods (n. d.). https://doi.org/10.1016/j.crmeth.2021.100105.

LeCun, Y., Bengio, Y., Hinton, G., 2015. Deep learning. Nature 521, 436–444. https://doi.org/10.1038/nature14539.

Lignani, G., Ferrea, E., Difato, F., Amarù, J., Ferroni, E., Lugarà, E., Espinoza, S., Gainetdinov, R.R., Baldelli, P., Benfenati, F., 2013. Long-term optical stimulation of channelrhodopsin-expressing neurons to study network plasticity. Front. Mol. Neurosci. 6, 22. https://doi.org/10.3389/fnmol.2013.00022.

Lilienberg, J., Hegyi, Z., Szabó, E., Hathy, E., Málnási-Csizmadia, A., Réthelyi, J.M., Apáti, Á., Homolya, L., 2021. Pharmacological modulation of neurite outgrowth in human neural progenitor cells by inhibiting non-muscle Myosin II. Front. Cell Dev. Biol. 9, 719636 https://doi.org/10.3389/fcell.2021.719636.

Long, B.L., Li, H., Mahadevan, A., Tang, T., Balotin, K., Grandel, N., Soto, J., Wong, S.Y., Abrego, A., Li, S., Qutub, A.A., 2017. GAIN: a graphical method to automatically analyze individual neurite outgrowth. J. Neurosci. Methods 283, 62–71. https://doi.org/10.1016/j.jneumeth.2017.03.013.

Lulevich, V., Shih, Y.-P., Lo, S.H., Liu, G.-Y., 2009. Cell tracing dyes significantly change single cell mechanics. J. Phys. Chem. B 113, 6511–6519. https://doi.org/10.1021/jp8103358.

Matsumoto, A., Agbariah, W., Nolte, S.S., Andrawos, R., Levi, H., Sabbah, S., Yonehara, K., 2021. Direction selectivity in retinal bipolar cell axon terminals. Neuron 109, 2928–2942.e8. https://doi.org/10.1016/j.neuron.2021.07.008.

Mattioni, M., Novère, N.L., 2013. Integration of biochemical and electrical signaling-multiscale model of the medium spiny neuron of the striatum. PLoS One 8, e66811. https://doi.org/10.1371/journal.pone.0066811.

NeuronJ, ImageJ Wiki (n.d.). ⟨https://imagej.github.io/plugins/neuronj⟩ (Accessed June 29, 2023).

Pai, V.P., Cooper, B.G., Levin, M., 2022. Screening biophysical sensors and neurite outgrowth actuators in human induced-pluripotent-stem-cell-derived neurons. Cells 11, 2470. https://doi.org/10.3390/cells11162470.

Pemberton, K., Mersman, B., Xu, F., 2018. Using ImageJ to ASsess Neurite Outgrowth in Mammalian Cell Cultures: Research Data Quantification Exercises in Undergraduate Neuroscience Lab. J. Undergrad. Neurosci. Educ. 16, A186–A194.

Ronneberger, O., Fischer, P., Brox, T., 2015. U-Net: convolutional networks for biomedical image segmentation. In: Navab, N., Hornegger, J., Wells, W.M., Frangi, A.F. (Eds.), Med. Image Comput. Comput. -Assist. Interv. – MICCAI 2015, Springe Int. Publ., Cham 234–241. https://doi.org/10.1007/978-3-319-24574-4_28.

Sacher, W.D., Chen, F.-D., Moradi-Chameh, H., Liu, X., Almog, I.F., Lordello, T., Chang, M., Naderian, A., Fowler, T.M., Segev, E., Xue, T., Mahallati, S., Valiante, T. A., Moreaux, L.C., Poon, J.K.S., Roukes, M.L., 2022. Optical phased array neural probes for beam-steering in brain tissue. Opt. Lett. 47, 1073–1076. https://doi.org/10.1364/OL.441609.

Shea, T.B., Perrone-Bizzozero, N.I., Beermann, M.L., Benowitz, L.I., 1991. Phospholipid-mediated delivery of anti-GAP-43 antibodies into neuroblastoma cells prevents neuritogenesis. J. Neurosci. 11, 1685–1690. https://doi.org/10.1523/JNEUROSCI.11-06-01685.1991.

Shrestha, P., Kuang, N., Yu, J., 2023. Efficient end-to-end learning for cell segmentation with machine generated weak annotations. Commun. Biol. 6, 1–10. https://doi.org/10.1038/s42003-023-04608-5.

Sordini, L., Garrudo, F.F.F., Rodrigues, C.A.V., Linhardt, R.J., Cabral, J.M.S., Ferreira, F. C., Morgado, J., 2021. Effect of electrical stimulation conditions on neural stem cells differentiation on cross-linked PEDOT:PSS Films. Front. Bioeng. Biotechnol. 9. ⟨https://www.frontiersin.org/articles/10.3389/fbioe.2021.591838⟩ (accessed June 12, 2023).

Stockley, J.H., Evans, K., Matthey, M., Volbracht, K., Agathou, S., Mukanowa, J., Burrone, J., Káradóttir, R.T., 2017. Surpassing light-induced cell damage in vitro with novel cell culture media. Sci. Rep. 7, 849. https://doi.org/10.1038/s41598-017-00829-x.

Stringer, C., Wang, T., Michaelos, M., Pachitariu, M., 2021. Cellpose: a generalist algorithm for cellular segmentation. Nat. Methods 18, 100–106. https://doi.org/10.1038/s41592-020-01018-x.

Su, Z., Kishida, S., Tsubota, S., Sakamoto, K., Cao, D., Kiyonari, S., Ohira, M., Kamijo, T., Narita, A., Xu, Y., Takahashi, Y., Kadomatsu, K., 2017. Neurocan, an extracellular chondroitin sulfate proteoglycan, stimulates neuroblastoma cells to promote malignant phenotypes. Oncotarget 8, 106296–106310. https://doi.org/10.18632/oncotarget.22435.

Su, H., Yin, Z., Huh, S., Kanade, T., 2013. Cell segmentation in phase contrast microscopy images via semi-supervised classification over optics-related features. Med. Image Anal. 17, 746–765. https://doi.org/10.1016/j.media.2013.04.004.

Szarowicz, C.A., Steece-Collier, K., Caulfield, M.E., 2022. New frontiers in neurodegeneration and regeneration associated with brain-derived neurotrophic factor and the rs6265 single nucleotide polymorphism. Int. J. Mol. Sci. 23, 8011. https://doi.org/10.3390/ijms23148011.

Torres-Espín, A., Santos, D., González-Pérez, F., del Valle, J., Navarro, X., 2014. Neurite-J: An Image-J plug-in for axonal growth analysis in organotypic cultures. J. Neurosci. Methods 236, 26–39. https://doi.org/10.1016/j.jneumeth.2014.08.005.

Vicar, T., Balvan, J., Jaros, J., Jug, F., Kolar, R., Masarik, M., Gumulec, J., 2019. Cell segmentation methods for label-free contrast microscopy: review and comprehensive comparison. BMC Bioinforma. 20, 360. https://doi.org/10.1186/s12859-019-2880-8.

Wu, G., Fang, Y., Lu, Z.-H., Ledeen, R.W., 1998. Induction of axon-like and dendrite-like processes in neuroblastoma cells. J. Neurocytol. 27, 1–14. https://doi.org/10.1023/A:1006910001869.

Xu, Y.K.T., Chitsaz, D., Brown, R.A., Cui, Q.L., Dabarno, M.A., Antel, J.P., Kennedy, T.E., 2019. Deep learning for high-throughput quantification of oligodendrocyte ensheathment at single-cell resolution. Commun. Biol. 2, 1–12. https://doi.org/10.1038/s42003-019-0356-z.

Zhou, Z., Kuo, H.-C., Peng, H., Long, F., 2018. DeepNeuron: an open deep learning toolbox for neuron tracing. Brain Inf. 5, 3. https://doi.org/10.1186/s40708-018-0081-2.